Vol. **107** (2005) *ACTA PHYSICA POLONICA A* No. 3

Magnetic Resonance Imaging at Low Magnetic Field Using Hyperpolarized ^{3}He Gas

M. Suchanek[a,*], K. Cieślar[a], T. Pałasz[a], K. Suchanek[a], T. Dohnalik[a] and Z. Olejniczak[b]

[a]M. Smoluchowski Institute of Physics, Jagiellonian University
Reymonta 4, 30-059 Kraków, Poland
[b]Institute of Nuclear Physics, Polish Academy of Sciences
Radzikowskiego 152, 31-342 Kraków, Poland

(Received November 24, 2004)

A low magnetic field magnetic resonance imaging system for small animal lung imaging using hyperpolarized ^{3}He gas is presented. The hyperpolarized ^{3}He gas at 1 mbar pressure and 30% polarization is obtained by the metastability exchange optical pumping technique. The magnetic resonance imaging unit is based on a permanent magnet of open geometry, built from a new generation Nd–B–Fe magnetic material. It produces the magnetic field of 88 mT with homogeneity better than 50 ppm in the 10 cm diameter sphere, after application of passive shimming. The magnetic field gradients of 30 mT/m are generated by a set of biplanar, actively shielded gradient coils. The first ^{1}H images of various biological objects, as well as ^{3}He images of the rat lung *in vivo* obtained in the described system are shown. In terms of sensitivity and resolution, the technique is superior to conventional ^{1}H magnetic resonance imaging, and offers great possibilities in early diagnosis of lung diseases.

PACS numbers: 32.80.Bx, 67.65.+z, 75.50.–y, 87.61.–c

1. Introduction

The polarization of nuclear spins in thermal equilibrium that is achievable at the magnetic field of 1 T at room temperature is of the order of 10^{-6}. The

*corresponding author; e-mail: suchanek@if.uj.edu.pl

magnetic resonance imaging (MRI) technique owes its great success in medical applications to high concentration of protons in biological tissues. This is not so in the case of human lungs, filled with atmospheric air, with low water vapor content. Therefore the proton MRI studies of human lungs are very difficult due to low sensitivity. In the view of the fact that lung diseases are the number four of mortality causes in Europe, it is of utmost importance to develop improved tools that could help in early diagnosis as well as in prognosis during the therapy.

It is well known that by optical pumping of ^{3}He one can create a nuclear polarization of the order of one, thus exceeding the thermal level by six orders of magnitude [1]. Such hyperpolarized ^{3}He gas can be mixed with ^{4}He and N_2 and inhaled by a patient, enabling highly sensitive imaging of the lungs with a good resolution. This was demonstrated for the first time in 1996 by Ebert et al. [2] and Bachert et al. [3], and successfully tested on animals and human subjects [4]. In spite of the low density of ^{3}He gas in the lungs (10^5 lower than that of protons in tissues), high resolution *in vivo* images of all air spaces, from the bronchial tree to the alveola, were obtained. The method is non-invasive and offers great possibilities for evaluating anatomy and physiology of lungs. The current imaging protocols include measurements of ventilation, perfusion, and diffusion in the lungs, as well as the breath-hold anatomical imaging. The animal models are developed to study drug effects on various lung diseases.

Since the large nuclear polarization of ^{3}He is obtained by optical means, it is possible to perform MRI at low magnetic field, without sacrificing sensitivity or resolution [5–7]. The main advantage of such approach is low initial investment and low operational cost, because the most expensive component of the standard MRI scanner, namely the superconducting magnet, is not necessary. The present paper describes a low field (88 mT) MRI system based on a permanent magnet for imaging small animal lungs using hyperpolarized ^{3}He gas, which is produced on-site by a compact table-top optical polarizer.

The paper is organized as follows. The design and performance of the ^{3}He optical polarizer based on the metastability exchange method is described in Sect. 2. A detailed description of the MRI system is presented in Sect. 3, with a special emphasis put on characteristic features needed for hyperpolarized ^{3}He application in low magnetic field. The optimization and testing procedures of the novel magnetic field and magnetic field gradients sources are described in great detail. The first proton and ^{3}He MRI images obtained in the system are shown in Sect. 4. The paper is concluded by discussion of future prospects for further improvement of the performance and for possible applications of the system in other areas of applied physics, biology, and medicine.

2. Gas production unit

The hyperpolarized ^{3}He is obtained in the metastability exchange optical pumping process [8, 9]. The low pressure ^{3}He gas ($\sim$ mbar) is placed in a guiding

magnetic field of the order of a few mT. In the first phase, the helium atoms in the $1\,^1S_0$ ground state are transferred to the $2\,^3S_1$ metastable state by the application of weak rf discharge. Then the optical pumping between the hyperfine sublevels of $2\,^3S$ and $2\,^3P$ state proceeds using the transition at $\lambda = 1083$ nm wavelength. As a result of the absorption of circularly polarized laser beam and hyperfine coupling the total angular momentum of the metastable atom becomes oriented. Nuclear polarization of the ground state ^{3}He atom builds up during so-called metastability exchange collisions. During the collisions the nuclear orientation remains unaffected while the electronic states of the atoms are exchanged. A continuous application of rf discharge and laser radiation leads to the equilibrium polarization, of magnitude dependent on laser power, helium gas pressure, and the relaxation rate. The maximum polarization that can be achieved by this method is about 80% [10].

Based on the above principle, a dedicated, table-top ^{3}He optical polarizer was built to produce hyperpolarized ^{3}He gas for MRI applications. A schematic diagram of the apparatus is sketched in Fig. 1. A homogeneous, 3 mT magnetic field B_0 is produced by a set of Helmholtz coils. A glass cylindrical cell, 5 cm long, 5 cm in diameter, is placed in the field center and used as the optical pumping cell. It is first evacuated by a system with the turbomolecular pump, and then filled with a few mbars of ^{3}He gas, using the gas handling system. A weak rf discharge is produced by two electrodes wrapped around the cell, which are driven by a 3 MHz, 10 W rf power amplifier, via a matching transformer. A distributed Bragg reflector (DBR) laser diode (SDL-6702-H1) delivering up to 50 mW of power is used for optical pumping. The pumping beam passes through the cell once and then is collected by a photodiode to monitor the light absorbed by metastable atoms. A typical curve, which indicates the changes in transmitted light intensity as the

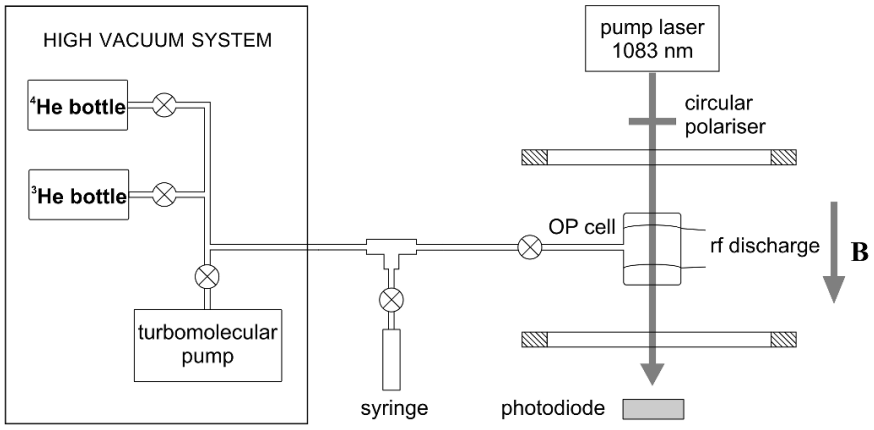

Fig. 1. A schematic diagram of the apparatus.

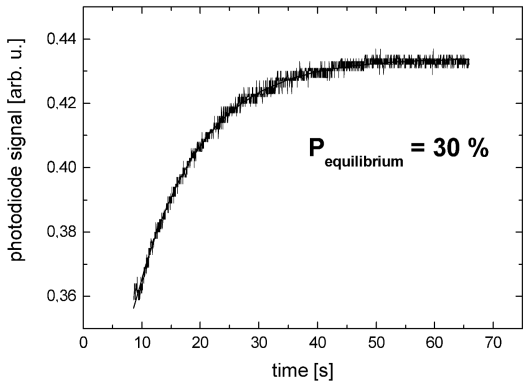

Fig. 2. The changes in transmitted light intensity during the polarization build-up for the $\sim$ 1 mbar helium pressure. The exponential curve was fitted with time constant 11 s. The laser power was 50 mW and the equilibrium polarization reached approximately 30%.

polarization builds up, is shown in Fig. 2. The equilibrium signal corresponds to about 30% of nuclear polarization for the $\sim$ 1 mbar ^{3}He gas pressure.

The nuclear polarization of ^{3}He gas in the optical pumping cell is measured both by the optical and NMR polarimeters. The optical method is based on the analysis of the degree of circular polarization of the 668 nm red light emitted by the discharge in the cell [11]. During the discharge sustained in the helium gas atoms can be transferred to the various excited levels with unperturbed nuclear spin. The hyperfine interaction in those states mixes the nuclear and electronic polarization. The result of this mixing turns up in spontaneous emission as a degree of circular polarization which is related directly to the nuclear orientation. In principle this technique can give an absolute polarization. In order to improve the sensitivity, the lock-in technique is used by applying a low frequency modulation to the rf discharge, and simultaneously using the modulation signal as the reference.

A dedicated, low frequency pulse NMR spectrometer was built to monitor the nuclear polarization of ^{3}He gas (Larmor frequency equal to 90 kHz). The transmitting coils of Helmholtz type are orthogonal to B_0 and produce a homogeneous B_1 rf field within the volume of the cell. The receiving coils consist of two square sections located very close to the cell, orthogonally both to B_0 and B_1, to reduce an rf coupling between the transmitter and receiver. Additionally, a third section of identical geometry but doubled number of turns is connected in series, in order to cancel out any external electromagnetic interference, which can be rather strong at such low resonance frequency. A small tilting angle rf pulse applied to the transmitting coil causes precession of nuclear magnetization. This in turn induces a free induction decay (FID) signal in the receiving coil which can be fed directly to the digital lock-in, owing to relatively low precession frequency. A proper gating circuitry protects the detection system during the rf pulse and

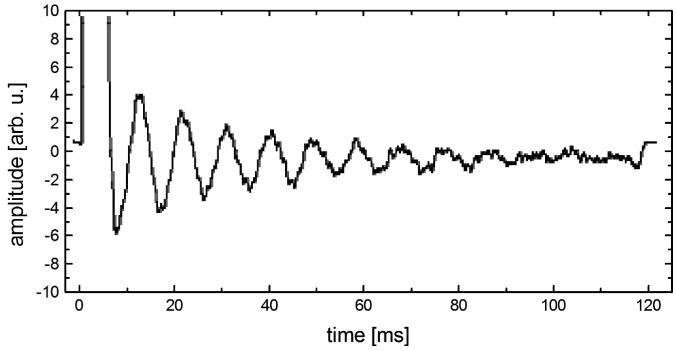

Fig. 3. A typical, slightly off-resonance FID signal from the optical pumping cell, measured at about 90 kHz by the NMR polarimeter.

turns off the rf discharge during the NMR data acquisition. A typical, slightly off--resonance NMR signal observed at the output of the NMR polarimeter is shown in Fig. 3. Although its amplitude provides only a relative measure of nuclear polarization, it can be calibrated against the optical polarimeter. It should be stressed that both polarimeters can monitor the dynamics of polarization without much interference with the process.

In order to evaluate the parameters of hyperpolarized ^{3}He gas in the actual MRI experiment, the optical pumping was temporarily setup in the center of 88 mT permanent magnet, and the NMR experiment on the hyperpolarized helium gas was performed using the MRI system (to be described in the following section). The laser beam parallel to the vertical B_0 field of magnet had to be delivered to the optical pumping cell by a set of mirrors. Relaxation time measurements were performed using two sealed cells filled with pure ^{3}He (2 mbar) and a mixture of ^{3}He/^{4}He (0.5 mbar/1.6 mbar). The spin–lattice relaxation time T_1 in the pure ^{3}He measured by a series of small tilting angle rf pulses was equal to 89 min, and T_2 measured by Carr–Purcell–Meiboom–Gill sequence [12] was 1.1 s. The relaxation times T_1 and T_2 measured in the ^{3}He/^{4}He mixture were equal to 34 min and 0.34 s, respectively. These parameters were found to be satisfactory for performing *in vivo* MRI experiments on the rat lungs.

For *in vivo* experiments the gas pressure of the order of 1 bar is needed. The cell was filled with 8 mbar of pure ^{3}He gas and polarized. The resulting FID obtained from the hyperpolarized helium gas is shown at the top of Fig. 4. A slow decay of the NMR signal represents a true spin–spin relaxation process with a time constant T_2, because the magnetic field inhomogeneity effects are averaged out by fast diffusion. In the next step, 1 bar of ^{4}He was added to 8 mbars of hyperpolarized ^{3}He. The resulting FID is shown at the bottom of Fig. 4. The amplitude of the signal is slightly smaller, probably due to some impurities introduced. The signal decays much faster, representing the dephasing process caused by magnetic field inhomogeneities, which are no longer averaged

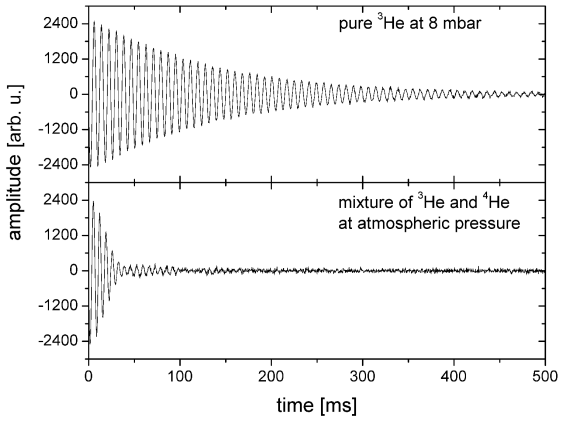

Fig. 4. FID signal observed by the NMR spectrometer at 2.84 MHz from pure ^{3}He at low pressure (top) and after adding about 1 bar of ^{4}He (bottom).

out at higher pressure and slower diffusion. The ^{3}He/^{4}He mixture was further extracted from the cell and used for animal studies to be described in Sect. 4.

3. MRI system

A low field MRI system for imaging small animal lungs using hyperpolarized ^{3}He consists of the permanent magnet producing the static field B_0, a set of biplanar, actively shielded gradient coils, the NMR console, and the rf coil. They are described in detail in the following subsections.

3.1. Permanent magnet

The permanent magnet of unique geometry was built from a new generation Nd–B–Fe magnetic material, which provides a very high magnetic energy density and a high coercivity [13]. The mechanical design of the magnet is shown in Fig. 5. Its open structure provides an easy access both for optical pumping equipment for *in situ* polarization of ^{3}He gas, and for the objects to be imaged. The magnets in the form of 48 pieces $10 \times 10 \times 2$ cm are located in two parallel planes. A special equipment was constructed to put the already magnetized pieces together and to assure sufficient accuracy of assembling the whole structure. The poles made of Armco homogenize the field generated by the magnets. An additional ring in the pole improves the central homogeneity even further. The distance between the poles is 25 cm, and the field homogeneity is optimized for the 10 cm diameter sphere. The magnetic flux is closed by four columns. The total weight of the magnet is about 1500 kg.

The magnet produces a magnetic field of 88 mT, with the inhomogeneity of 360 ppm in the 10 cm diameter sphere, instead of 100 ppm that was initially

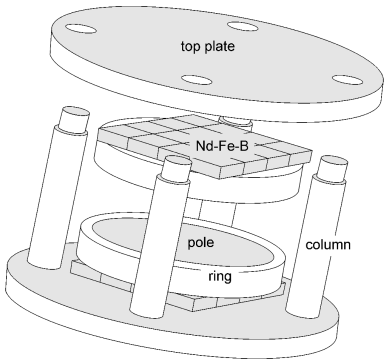

Fig. 5. A schematic view of the 88 mT permanent magnet structure.

assumed. According to simulations, the main source of the error was an insufficient precision in placing the pole plates in parallel, which was less than assumed 0.05 mm. A special NMR field mapping device was constructed to measure the field map accurately. A spherical, 3 mm diameter water sample could be placed anywhere in the working volume with 0.5 mm precision and the magnetic field could be measured with about 1 ppm accuracy. The original magnetic field distribution on the surface of 10 cm diameter sphere and on the z axis is shown on the left and right side of the top part of Fig. 6, respectively. The dominant source of error is the z^2 axial harmonic. The analysis of the field map in terms of spherical harmonics up to the sixth order led to the calculation of masses and positions of compensating steel pieces that could be attached to the surfaces of the magnet poles. That method of passive shimming was found to be optimal [14]. The only complication was caused by a low value of the main magnetic field, which was not sufficient to saturate the iron pieces. Therefore, the demagnetizing factor had to be determined experimentally for a given shape of the correcting pieces, and the shapes had to be kept the same for all pieces, independently of their masses. They were in the form of cylinders with height to diameter ratio equal to 5/8.

About 50 steel pieces were used in the first iteration of shimming. The inhomogeneity was reduced to about 42 ppm, instead of expected 30 ppm. The field map obtained after the first iteration is shown at the bottom part of Fig. 6, using the same vertical scale as before. The field analysis in terms of spherical harmonics showed no dominant component. After a thorough discussion of possible sources of errors, such as generation of magnetic images in the non-saturated poles, localization errors, mutual effects between closely spaced pieces, and other nonlinear effects, it was concluded that the main cause of errors was the precision in machining the pieces. It was of the order of 1% and should be improved to about 0.2% in order to achieve the required 10 ppm inhomogeneity. The present value puts the lower limit on the gradient strength that can be used in the imaging sequences.

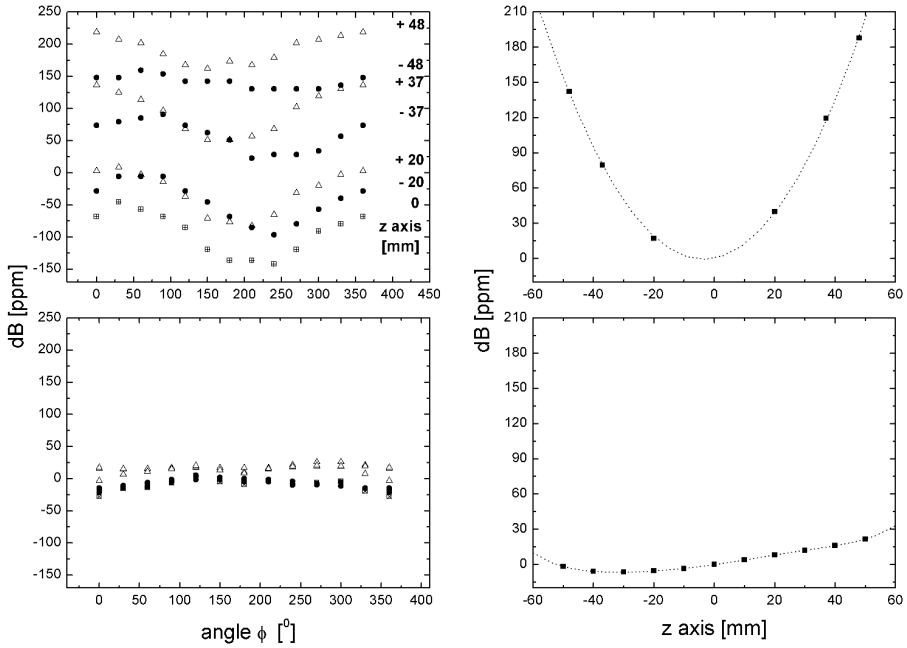

Fig. 6. The magnetic field distribution within the working volume on the surface of 10 cm diameter sphere (left), on the z axis (right), before (top) and after shimming (bottom). The different point shapes correspond to consecutive cross-sections through the working volume sphere in the z direction.

Due to the low Curie temperature of the magnetic material used in the construction of the permanent magnet, the temperature dependence of the magnetic field was about –836 ppm/K, which was unacceptable in the MRI applications. Therefore it was necessary to stabilize the temperature of the magnet. That was achieved by building an air conditioning system in the laboratory, which was necessary anyway for performing animal studies. The temperature in the laboratory was kept constant to ± 1 K. Additionally, the magnet was put inside the Faraday cage, in which the temperature was stabilized by an independent system to ± 0.1 K. The Faraday cage simultaneously provides sufficient electromagnetic shielding at a relatively low resonance frequency of 2.8 MHz for ^{3}He. It is made of 0.5 mm thick copper sheets soldered together and mounted on an aluminum frame.

However, the field stability was still not satisfactory for our purpose. The final temperature compensation was achieved by using a current feedback system and the temperature sensor anchored to the magnet pole. A strong correlation between the magnetic field variations and the temperature measured by the sensor is illustrated on the left of Fig. 7. Hence the signal from the temperature sensor could be used to control the current in the B_0 coil that is incorporated in the gradient coil set. That way the residual, long-term temperature variation of the

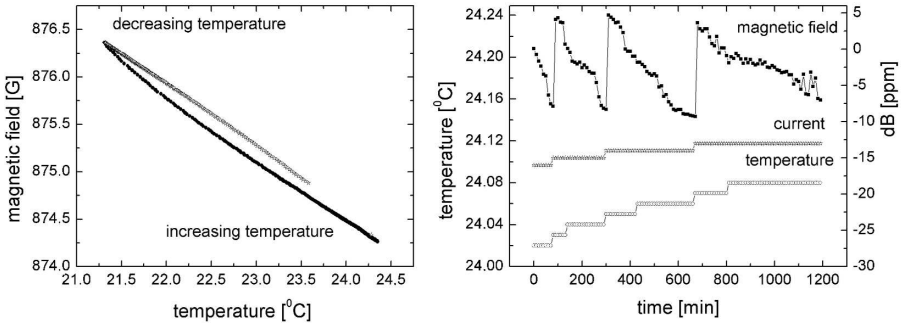

Fig. 7. Correlation between the magnetic field variations and the temperature measured by the sensor anchored to the magnet pole (left) and long-term field stability achieved by using a current feedback system (right).

magnetic field was reduced to below 15 ppm, as can be seen on the right of Fig. 7. It is limited by the sensitivity of the temperature sensor (0.01 K), and the resolution of the digitally controlled current source (10 mA).

3.2. Gradient coils

The magnetic field gradients are generated by a set of biplanar, actively shielded gradient coils. Due to the close vicinity of conducting surfaces of the poles, the active shielding was necessary to minimize the eddy currents effects. The overall layout of the coils located in the upper set is shown in the Table, in the form of the schematic cross-section. Each gradient coil has its counterpart that generates an opposite field at the surface of the pole. That way the magnetic field at the surface of the pole is reduced by about a factor of 10, as compared to the nonshielded case. Additionally, a B_0 coil is included for the main field correction, and a space for water cooling is provided in the middle of the set. There is also an open space left between the gradient assembly and the magnet pole to allow for passive shimming and air cooling. A typical current pattern for the transverse gradient coil and the corresponding shielding coil is shown on the left and right of Fig. 8, respectively.

The linearity of the gradients within the working volume, measured by the same method as used before for measuring the main field map, was found to be within the required limit of 1% for all three directions. The gradient coils are driven by three Resonance Research 40 A/100 V gradient amplifiers. The gradient strengths are about 30 mT/m at the current of 40 A, for all three directions. The minimum rise time for the gradient pulses is set to 200 μs. The gradient coils are cooled by temperature stabilized water circulating in the closed circuit, and by the forced air circulation between the gradient coils assembly and the magnet poles. An additional interface unit was built between the NMR console and the gradient amplifiers to use the gradient coils for final manual or automatic active shimming.

TABLE

The layout of the gradient coils.

Layer	Thickness [mm]
space for shimming	3.4
air cooling	5
x, y, z shielding coils each separated by the layer of laminate and adhesive	12.529
bond	0.25
tubes for water cooling	7.35
bond	0.25
B_0 coil	0.8128
x, y, z gradient coils each separated by the layer of laminate and adhesive	13.577
bond	0.6146
rf shield separated by the layer of laminate and adhesive	0.951
TOTAL	44.7344

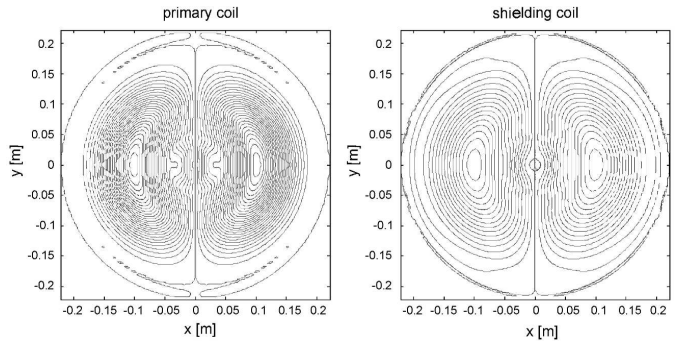

Fig. 8. The current pattern for the transverse gradient coil (left) and the corresponding shielding coil (right).

The method used to monitor eddy current effects caused by the switching gradients is similar to the one described by Bartusek and Puczok [15]. The pulse sequence is shown in Fig. 9. The resonance offset of the acquired FID was measured as a function of delay between the trailing edge of the gradient pulse and the beginning of acquisition. The gradient pulse was sufficiently long for the transients caused by the leading edge to decay to zero, so only the trailing edge effects were measured. The dynamic frequency offset was referenced to the value measured after 500 ms, to exclude the temperature drift effects. Typical eddy current field maps measured by the method described above are shown in Fig. 10. The first

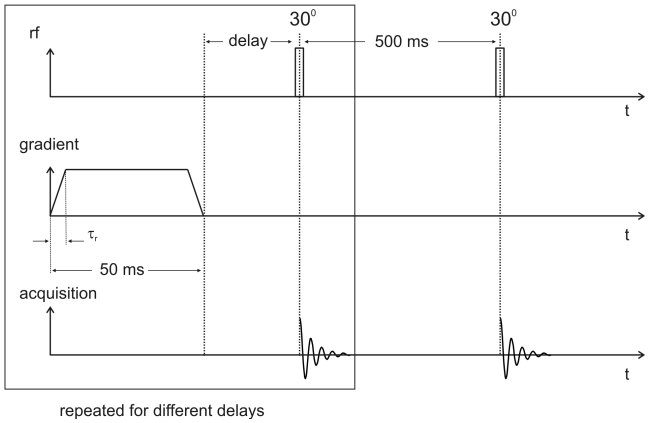

Fig. 9. The pulse sequence used for measuring the eddy current effects caused by the switching magnetic field gradients.

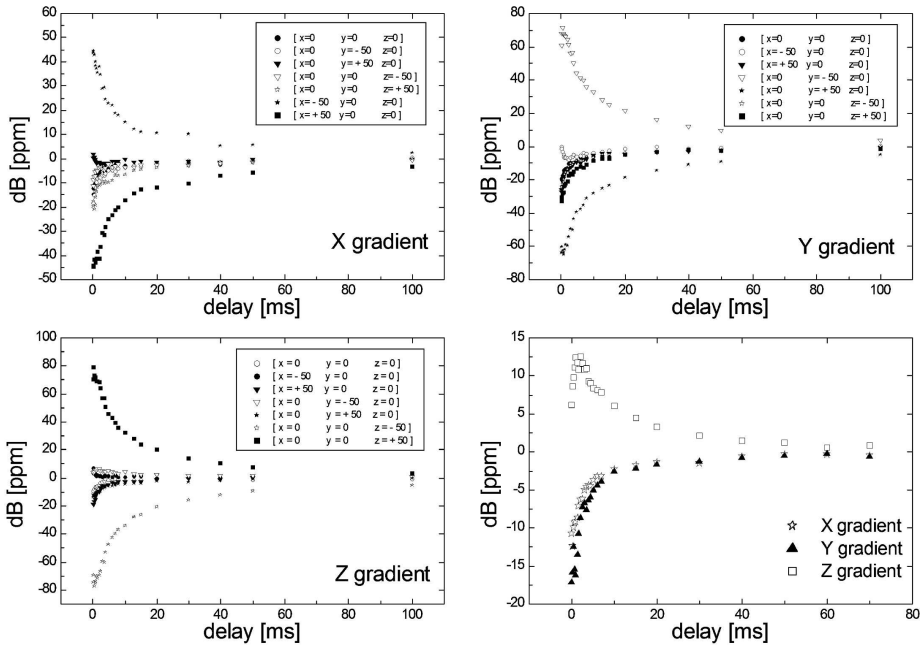

Fig. 10. Eddy current field maps obtained by using a 3 mm diameter water sample placed at various locations for gradient X (top left), Y (top right), Z (bottom left), and using a large, 10 cm cylindrical water sample located in the center of the magnet (bottom right).

three figures present the data obtained by using a 3 mm diameter water sample, so the spatial eddy currents effects could be monitored, for each direction of the gradient, separately. The largest dynamic field variations occur on the axis cor-

responding to the applied gradient direction, as expected. The fourth figure was obtained by using a large, 10 cm cylindrical water sample, so the integral eddy current effects could be estimated. The residual time dependent fields amplitudes due to the eddy currents generated in the magnet poles are 20 ppm and decay with the time constant of about 20 ms for each gradient direction, when the maximum amplitude gradient pulse with a minimum rise time is used, without preemphasis.

3.3. NMR console and rf coil

The NMR console consists of a commercial MR Research Systems (previously SMIS) MR4200 Narrow Band console supplemented by a home-built frequency converter, which makes it possible to perform the experiments on either ^{3}He or proton frequencies. The standard library of imaging sequences has been enhanced by special imaging protocols that are suitable for imaging small animal lungs using hyperpolarized ^{3}He.

The transmitting/receiving rf coil is a solenoid supplemented by an additional pair of paraxial coils, which compensates the field up to the 6th order, producing the B_1 field within the working volume of better than 1% homogeneity [16]. The coil was designed to take advantage of the whole working volume. Its internal diameter of 120 mm is large enough to incorporate a small animal for imaging, or the optical pumping cell, so that the magnitude and dynamics of the polarization can be monitored *in situ*. In order to improve the filling factor, hence the signal-to-noise ratio (SNR), a second, cylindrical rf coil of 80 mm internal diameter was also constructed for imaging the rat lungs. Both coils can be quickly switched between the ^{3}He and proton resonance frequency, so that the complementary images can be obtained on the same object. The rf coils are driven by the Dressler 1 kW rf power amplifier via a matching circuit and a passive duplexer, isolating the detector during the rf pulse. The NMR signal induced in the rf coil is first amplified by a low noise preamplifier (AU-1583) made by MITEQ company, and then fed to the rf unit of the NMR console.

4. Results and discussion

The performance of the MRI scanner was evaluated on proton images of phantoms and small biological objects. The spatial resolution achieved was measured to be better than 1 mm. The linearity and SNR of the images were tested using simple gradient echo (GE) and spin echo (SE) sequences. Then the fast MRI sequences such as FSE (fast SE) [17] and FLASH (fast, low angle shot) [18] were implemented and successfully tested. Typical proton transverse and sagittal slices obtained using FSE are shown in Fig. 11. The acquisition parameters are given in the figure caption.

When performing ^{3}He MRI one has to take into account the fact that the nuclear polarization obtained via optical methods is non-renewable, and it decays

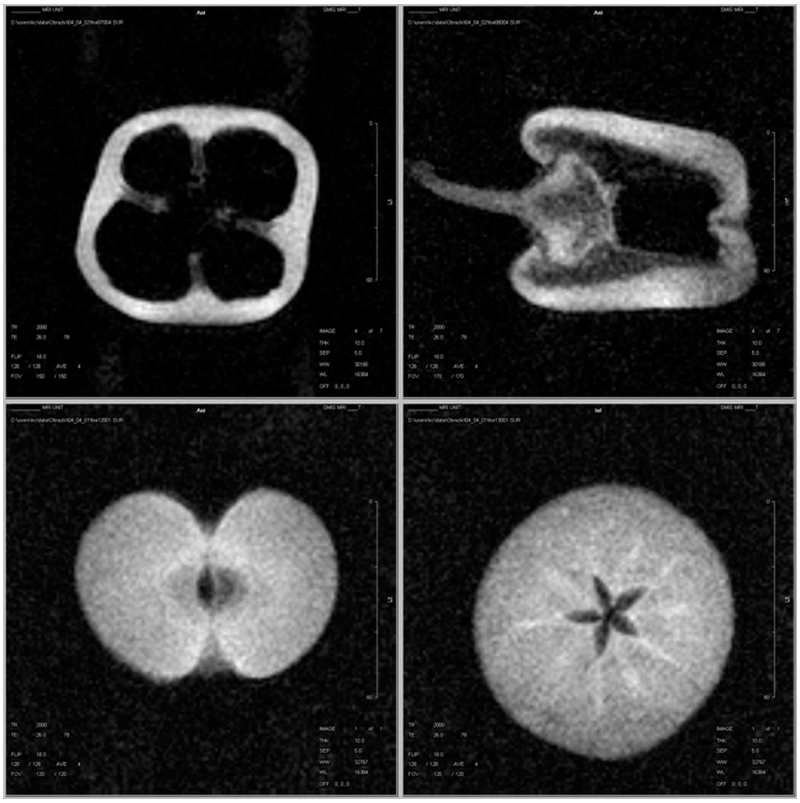

Fig. 11. Proton images of a red pepper (top) and an apple (bottom) obtained using FSE, 4 views per segment. Matrix size 128 × 128, field of view 150 mm, slice thickness 10 mm, sampling 10 kHz, echo time 26 ms, 4 averages, repetition time 2 s, total acquisition time 256 s.

within tens of seconds in the rat lungs. For this reason the FLASH sequence was used in all ^{3}He experiments, with a flip angle of about 6^0 and total acquisition time of less than 4 s. Test images of the glass cell filled with a mixture of ^{3}He and ^{4}He gas were obtained, then the image of a syringe that was used as the gas applicator, and of a small balloon that was emulating the rat lung. Finally, *in vivo* MRI experiments of the rat lungs were performed. The animal was anaesthetized, tracheotomized, and placed supine in the center of the rf coil. A volume of about 7 cm^3 of polarized gas was introduced from the syringe into the rat lungs via the trachea catheter. The images taken after two consecutive breaths are presented on the left and right of Fig. 12, respectively. During the first breath only one lung was filled with polarized ^{3}He. In spite of low spatial resolution of these images, one can easily recognize the characteristic shape of the rat lungs.

These preliminary results confirm the usefulness of low magnetic field MRI for both ^{3}He and ^{1}H imaging. The visualization of air spaces by using hyperpo-

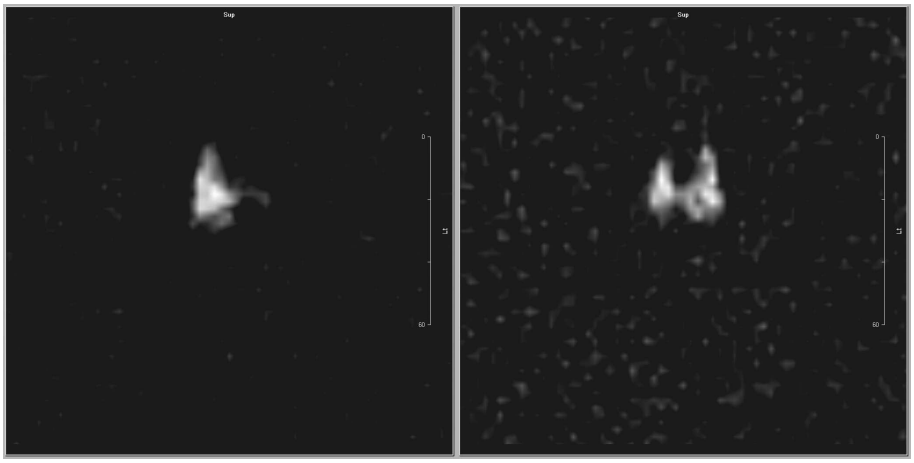

Fig. 12. First *in vivo* hyperpolarized ^{3}He gas image of the rat lungs, obtained using FLASH. Matrix size 128 × 128, field of view 150 mm, slice thickness 80 mm, sampling 5 kHz, flip angle 6°, echo time 16 ms, repetition time 30 ms, no averaging, total acquisition time 3.8 s.

larized ^{3}He gas provides anatomical information which is complementary to the standard ^{1}H MRI. A simultaneous proton and helium imaging of the same object is straightforward.

There is a room for many improvements of the system in order to obtain better SNR and spatial resolution of ^{3}He images. First of all, larger amounts of hyperpolarized ^{3}He is needed, characterized by higher pressure and larger total polarization. A new optical polarizer is being built for that purpose, which contains a novel ^{3}He compressor [19]. The helium gas polarized in the optical pumping cell at a few mbars will be compressed to about 100 mbars and transferred to a storage cell, also located in a homogeneous magnetic field. The final step will be the construction of a portable optical polarizer for on-site hyperpolarized ^{3}He production, which will be equipped with a higher power laser and will work in the hospital, using a high magnetic field available in the medical MRI scanner [20].

Several improvements of the MRI system are also planned. The temperature drift of the magnetic field will be eliminated by using a field-lock device. A second iteration of passive shimming will hopefully reduce the main field inhomogeneity in the working volume to below 10 ppm. The temporal characteristics of the magnetic field gradient system will be improved by the implementation of the preemphasis unit. Single-shot spiral and radial imaging sequences will complement the present library, which will allow for faster image acquisition. The ultimate goal is to use the experience gained in the construction of the prototype in designing a whole body MRI system for human lung imaging. The main advantage of such unit would be low investment and low operational costs, when compared with the standard MRI system based on the superconducting magnet.

Apart from small animal lung imaging, other applications of the presented system can be envisioned. They include animal studies of new contrast agents for MRI, diffusion studies in porous materials and zeolites [21], and standard proton imaging of medium-size heterogeneous objects. The open geometry of the magnet makes it ideal for *in situ* studies of molecular dynamics and diffusion taking place during the model catalytic processes. Such experiments are under preparation in our laboratory.

Acknowledgments

The table-top optical polarizer as well as the monitoring and control system were built in close cooperation with P.J. Nacher and his group from ENS, Paris, France. The permanent magnet was designed and built by K. Turek from the University of Science and Technology in Kraków. Z. Starčuk and B. Tomanek from the Institute for Biodiagnostics, NRC, Winnipeg, Canada, designed and built the gradient coils. D. Hoult from the Institute for Biodiagnostics, NRC, Winnipeg, Canada, was guiding us in shimming the permanent magnet. We also thank A. Jasiński for his contribution in assembling the MRI console, and K. Majcher and P. Marcinek for their help in animal preparations. This work was supported in part by the E.C. Fifth Framework Program (PHIL project QLG1-2000-01559), the State Committee for Scientific Research (Poland) (grant no. 158/E-338/SPUB-M/5 PR UE/DZ 82/2001-03), and the Polish Science Foundation (SUBIN no. 17/98, MILAB no. 40/2002).

References

[1] F.D. Colegrove, L.D. Schearer, G.K. Walters, *Phys. Rev.* **132**, 2561 (1963).

[2] M. Ebert, T. Grossmann, W. Heil, E.W. Otten, R. Sarkau, M. Leduc, P. Bachert, M.V. Knopp, L.R. Schad, M. Thelen, *Lancet* **34**, 1297 (1996).

[3] P. Bachert, L.R. Schad, M. Bock, M.V. Knopp, M. Ebert, T. Grossmann, W. Heil, D. Hoffman, R. Surkau, E.W. Otten, *Magn. Reson. Med.* **36**, 192 (1996).

[4] H.E. Moller, X.J. Chen, B. Saam, K.D. Hagspiel, G.A. Johnson, T.A. Altes, E.E. de Lange, H.-U. Kauczor, *Magn. Reson. Med.* **47**, 1029 (2002).

[5] G.P. Wong, C.H. Tseng, V.R. Pomeroy, R.W. Mair, D.P. Hinton, D. Hoffman, R.E. Stoner, F.W. Hersman, D.G. Cory, R.L. Walsworth, *J. Magn. Reson.* **141**, 217 (1999).

[6] L. Darrasse, G. Guilliot, P.-J. Nacher, G. Tastevin, *C.R. Acad. Sci. (Paris)* **324**, 691 (1997).

[7] Ch.P. Bidinosti, J. Choukeife, P.-J. Nacher, G. Tastevin, *J. Magn. Reson.* **162**, 122 (2003).

[8] P.-J. Nacher, M. Leduc, *J. Phys. (France)* **46**, 2057 (1985).

[9] K. Suchanek, K. Cieślar, T. Dohnalik, Z. Olejniczak, T. Pałasz, M. Suchanek, to be published.

[10] T.R. Gentile, R.D. McKeown, *Phys. Rev. A* **47**, 456 (1993).

[11] E. Stoltz, B. Villard, M. Meyerhoff, P.-J. Nacher, *Appl. Phys. B* **63**, 635 (1996).

[12] S. Meiboom, D. Gill, *Rev. Sci. Instrum.* **29**, 688 (1959).

[13] D. Brown, B.-M. Ma, Z. Chen, *J. Magn. Magn. Mater.* **248**, 432 (2002).

[14] F. Romeo, D.I. Hoult, *Magn. Reson. Med.* **1**, 44 (1984).

[15] K. Bartusek, V. Puczok, *Meas. Sci. Technol.* **4**, 357 (1993).

[16] M. Friedman, R. Avida, J. Brandstadter, G. Erez, *J. Phys. E. Sci. Instrum.* **17**, 212 (1984).

[17] J. Henning, A. Naureth, H. Friedburg, *Magn. Reson. Med.* **3**, 823 (1986).

[18] A. Haase, J. Frahm, D. Matthaei, W. Hanicke, K.-D. Merboldt, *J. Magn. Reson.* **67**, 258 (1986).

[19] J. Choukeife, X. Maitre, P.-J. Nacher, G. Tastevin, *Magn. Res. Mat. in Phys., Biol., Med., Suppl. 1 to* **15**, 201 (2002).

[20] M. Abboud, A. Sinatra, X. Maitre, G. Tastevin, P.-J. Nacher, *Europhys. Lett.* **68**, 480 (2004).

[21] G. Tastevin, P.-J. Nacher, J. Choukeife, *Physica B* **329-333**, 303 (2003).